Ann Nucl Med (2007) 21:537–543
DOI 10.1007/s12149-007-0057-4

TECHNICAL NOTE

Accelerated 3D-OSEM image reconstruction using a Beowulf PC cluster for pinhole SPECT

Tsutomu Zeniya · Hiroshi Watabe · Antti Sohlberg
Hidehiro Iida

Received: 18 May 2007 / Accepted: 6 August 2007

Abstract
Objective A conventional pinhole single-photon emission computed tomography (SPECT) with a single circular orbit has limitations associated with non-uniform spatial resolution or axial blurring. Recently, we demonstrated that three-dimensional (3D) images with uniform spatial resolution and no blurring can be obtained by complete data acquired using two-circular orbit, combined with the 3D ordered subsets expectation maximization (OSEM) reconstruction method. However, a long computation time is required to obtain the reconstruction image, because of the fact that 3D-OSEM is an iterative method and two-orbit acquisition doubles the size of the projection data. To reduce the long reconstruction time, we parallelized the two-orbit pinhole 3D-OSEM reconstruction process by using a Beowulf personal computer (PC) cluster.
Methods The Beowulf PC cluster consists of seven PCs connected to Gbit Ethernet switches. Message passing interface protocol was utilized for parallelizing the reconstruction process. The projection data in a subset are distributed to each PC. The partial image forward- and back-projected in each PC is transferred to all PCs. The current image estimate on each PC is updated after summing the partial images. The performance of parallelization on the PC cluster was evaluated using two independent projection data sets acquired by a pinhole SPECT system with two different circular orbits.
Results Parallelization using the PC cluster improved the reconstruction time with increasing number of PCs. The reconstruction time of 54 min by the single PC was decreased to 10 min when six or seven PCs were used. The speed-up factor was 5.4. The reconstruction image by the PC cluster was virtually identical with that by the single PC.
Conclusions Parallelization of 3D-OSEM reconstruction for pinhole SPECT using the PC cluster can significantly reduce the computation time, whereas its implementation is simple and inexpensive.

Keywords Pinhole SPECT · Image reconstruction · 3D-OSEM · PC cluster · Parallel computing

T. Zeniya (✉) · H. Watabe · A. Sohlberg · H. Iida
Department of Investigative Radiology, Advanced Medical Engineering Center, National Cardiovascular Center Research Institute, 5-7-1 Fujishiro-dai, Suita 565-8565, Japan
e-mail: zeniya@ri.ncvc.go.jp

Introduction

Small animal single-photon emission computed tomography (SPECT) allows in vivo high-resolution three-dimensional (3D) imaging of physiological functions in small animals. This facilitates an objective assessment of the pharmaceutical development and regenerative therapy in pre-clinical studies [1–8]. However, a conventional pinhole SPECT with single circular orbit has major limitations associated with non-uniform spatial resolution or axial blurring [1, 9]. This blurring can be moderated by applying statistical image reconstruction methods such as maximum likelihood expectation maximization (MLEM) [10] or ordered subsets expectation maximization (OSEM) [11] rather than Feldkamp's filtered back-projection (Feldkamp-FBP) method [12], but still remains problematic at the periphery of field of view [1, 9]. Recently, we have demonstrated that the uniformity of spatial resolution can be improved by complete projection data acquired with two different circular orbits [13, 14] that satisfy data completeness condition

of Tuy [15], combined with 3D-OSEM. However, a long computation time is required to obtain the reconstructed image because 3D-OSEM is an iterative method and two-circular orbit acquisition doubles the size of the projection data. To reduce the long reconstruction time, we parallelized the two-orbit 3D-OSEM reconstruction process by using a personal computer (PC) cluster. Several investigators have demonstrated speed-up of 3D-OSEM reconstruction in positron emission tomography (PET) [16–19] and SPECT [20]. This study was aimed at improving the speed of the computing time for two-orbit pinhole 3D-OSEM reconstruction. We have previously succeeded in improving the performance of motion correction for PET using a Beowulf PC cluster [21]. Beowulf PC cluster (http://www.beowulf.org) is defined as a cluster of several PCs running a free-software operating system such as Linux or FreeBSD, interconnected by an Ethernet or Myrinet network. Therefore, this cluster system can be extremely inexpensively built compared with conventional super computer systems. In this study, we implemented two-orbit pinhole 3D-OSEM on our Beowulf PC cluster. To test the performance of the PC cluster, actual data were processed and compared with results obtained by a single PC.

Materials and methods

PC cluster

The Beowulf-type PC cluster consists of seven PCs. There are four 2.4 GHz Xeon processors for a master PC and dual 1.4 GHz Pentium III processors for six slave PCs connected to Gbit Ethernet switches (Fig. 1, Table 1). Each PC has 1 GB physical memory. For the parallelizing task, we installed the local area multicomputing (LAM) 6.5.7 version of the message passing interface (MPI) protocol (http://www.lam-mpi.org) on each PC.

Table 1 Specification of our Beowulf personal computer (PC) cluster

Component	Specification
Master PC	PowerEdge 2650 (Dell) 4 Xeon (Intel) 2.4 GHz 1 GB physical memory Linux 2.4.18 operating system
Slave PCs (six)	PowerEdge 1650 (Dell) Dual Pentium III (Intel) 1.4 GHz 1 GB physical memory Linux 2.4.18 operating system
Switching hub	SuperStack 3 Switch 4900 (3COM) 12 × 1000BASE-T port

The program for this system was written in the C language (gcc version 2.96) on a Linux operating system (version 2.4.18).

Theory of formulation for parallelizing two-orbit pinhole 3D-OSEM reconstruction

Figure 2 shows a schematic diagram of two-orbit pinhole SPECT geometry and two-orbit 3D-MLEM iterative reconstruction. The two-orbit 3D-MLEM update can be expressed as

$$\lambda_j^{k+1} = \frac{\lambda_j^k}{\sum_{l=1}^{2}\sum_{i=1}^{n} C_{lij}} \sum_{l=1}^{2}\sum_{i=1}^{n} \frac{y_{li} C_{lij}}{\sum_{j=1}^{m} C_{lij}\lambda_j^k}, \quad (1)$$

where λ_j^k is the value of the image voxel j for the kth iteration, y_{li} is the measured value of the projection pixel i for the lth orbit, and C_{lij} is the probability of detecting a photon originating from image voxel j at projection pixel i for the lth orbit. Each iteration of the MLEM algorithm for two orbits consists of the following four steps: (1) forward-projecting current image estimate λ_j^k for two orbits (forward-projection), (2) dividing the measured and forward projections for two orbits (correction), (3) back-projecting corrections for two orbits (back-projection), and (4) generating λ_j^{k+1} with the back-projected image. A 3D voxel-driven projector using bilinear interpolation on the detector plane was employed in both the back- and forward-projections.

The ordered subsets (OS) scheme was used to reduce the number of iterations, and subsets were evenly divided for both orbits. In our earlier studies [13, 14], as 120

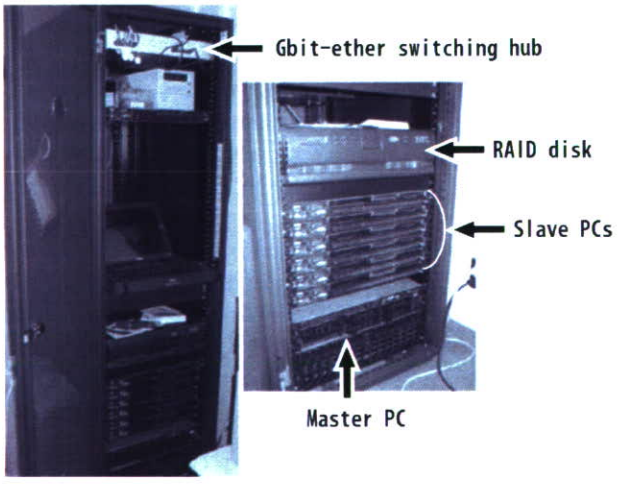

Fig. 1 Photograph of our Beowulf personal computer (PC) cluster

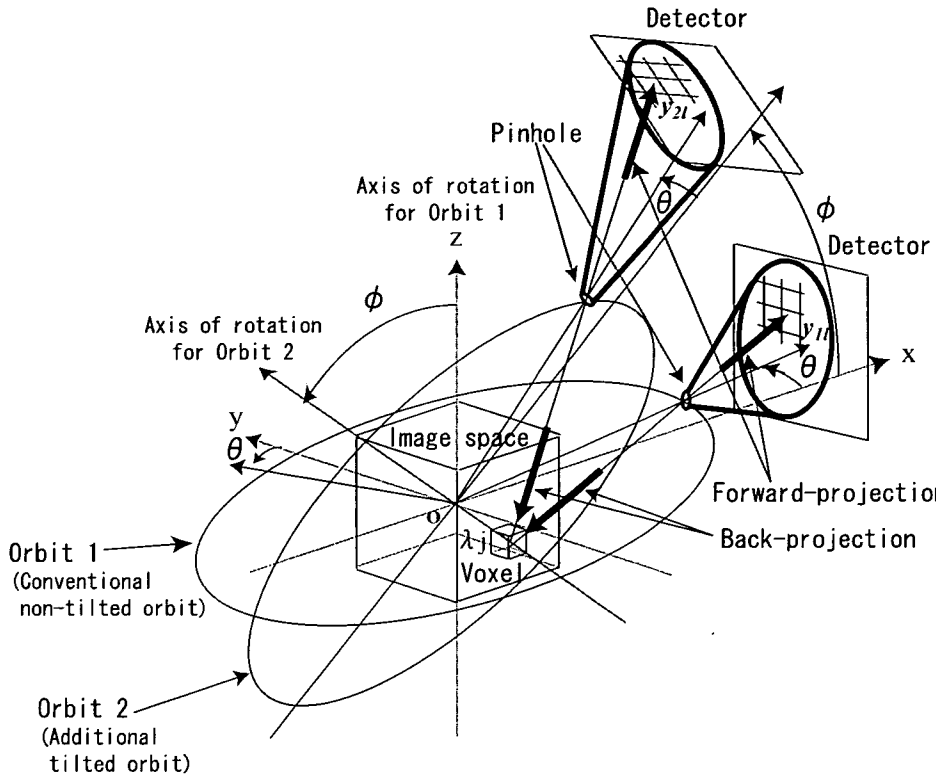

Fig. 2 Schematic diagram of geometry and three-dimensional ordered subsets expectation maximization (3D-OSEM) iterative image reconstruction in the pinhole single-photon emission computed tomography system with two-circular orbit

```
for all Iterations {
    for all Subsets{
        for (Views/Subsets) × Orbits on each PC {        Process 1: in parallel
            Forward-project current image estimate
            Calculate correction (measured projection / forward projection)
            Back-project correction
        }
        Sum partial back-projeced images on all PCs      Process 2: synchronization
        Update current image estimate (image ← image × backprojected image)
    }
}
```

Fig. 3 Pseudocode of parallelized 3D-OSEM for two orbits

projections for single orbit or 240 projections for two orbits were acquired and the current image estimate was updated with 8 subsets, 15 or 30 projections were assigned to one subset (i.e., data of $\theta = 0°, 24°, 48°, 72°, \ldots, 336°$ from both orbits were used to form the first subset).

We applied the projection space decomposition (PSD) [18] for parallelizing the two-orbit pinhole 3D-OSEM reconstruction. This method operates projection data in a block of a view. Figure 3 shows a pseudocode of parallelized 3D-OSEM for two orbits. Process 1 in Fig. 3 can be parallelized because the forward- and back-projection

Table 2 Distribution of 30-projection data in first subset to seven-PC cluster

PC number	Projection number (orbit number)				
1	1 (1)	57 (1)	113 (1)	49 (2)	105 (2)
2	9 (1)	65 (1)	1 (2)	57 (2)	113 (2)
3	17 (1)	73 (1)	9 (2)	65 (2)	
4	25 (1)	81 (1)	17 (2)	73 (2)	
5	33 (1)	89 (1)	25 (2)	81 (2)	
6	41 (1)	97 (1)	33 (2)	89 (2)	
7	49 (1)	105 (1)	41 (2)	97 (2)	

operations associated with each view are independent and can therefore proceed in parallel. At the end of each subset, a partial back-projected image is generated on each PC and these partial images are transferred to all PCs and then summed, to obtain the complete back-projected image (Process 2 in Fig. 3). Image synchronization is required for Process 2. Initial image estimates are loaded on memory on all PCs. The MPI library was used to implement this parallelization. In the MPI protocol, an identical program runs on independent PCs, with their interactions controlled by exchanging messages.

Figure 4 shows the distribution of 15 projections in one subset for single orbit in the case of total 120 projections. Table 2 shows the distribution of 30 projections in the subset for two orbits when seven PCs are used. As

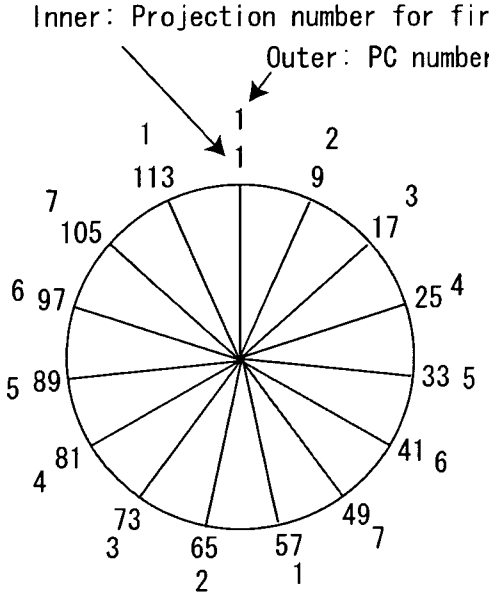

Fig. 4 Distribution of 15-projection data in the first subset for single orbit to seven-PC cluster

shown in Table 2, one PC needs to compute all 30 projections by itself, whereas with seven PC cluster each node uses five projections.

Performance evaluation using pinhole SPECT data

To evaluate the effects of parallelization, data obtained from previous phantom study were used. Detailed descriptions of the pinhole SPECT system were reported previously [13, 14]. This system consisted of a rotating object stage, a fixed conventional SPECT gamma camera (GCA-7100A, Toshiba, Tokyo, Japan) equipped with a pinhole collimator. The system can acquire two independent projection data sets with two different circular orbits to satisfy the completeness condition of Tuy. The rotating stage held the object vertically at tilted angles of $\phi = 0°$ and 45° to satisfy Tuy's condition. A multiple-disk phantom with ^{99m}Tc solution was used to evaluate axial blurring and resolution uniformity [13]. Projection data were acquired for 120 angular views in 3° steps for both orbits, in a 128 × 128 matrix with 16-bit integers. After decay correction, the total size of 240-projection data for two orbits with 32-bit floating point numbers was 15.7 MB. The projection data were reconstructed with eight subsets and two iterations, in a 128 × 128 × 128 matrix with 32-bit floating point numbers (8.4 MB).

Time for reconstruction was measured using different numbers of PCs from one to seven to evaluate the performance of the PC cluster. These measurements were repeated 10 times and the averaged reconstruction time was computed. For reference, the reconstruction time by non-iterative single-orbit Feldkamp-FBP approach was also measured. Feldkamp-FBP program provided by Toshiba was used in this study. The images reconstructed by the PC cluster and single PC were compared to verify whether they equaled. The difference of the two images was evaluated voxel by voxel by calculating the reconstruction error as

$$\varepsilon = \max_j \frac{|\lambda_j^S - \lambda_j^M|}{\lambda_j^S} \times 100(\%), \quad (2)$$

where λ_j^S is the voxel value of image obtained with single PC and λ_j^M obtained by PC cluster.

Results

Figure 5 shows the relationship between the number of PCs and the reconstruction time. The reconstruction time was reduced by increasing the number of PCs. The reconstruction time was 54 min and 18 s with a single PC, and was reduced to 10 min and 2 s with PC cluster. The speed-up factor was approximately 5.4. In this study, the reconstruction time with seven PCs was not improved compared with that with six PCs. The reconstruction time using single-orbit Feldkamp-FBP was 2 min and 44 s. The long reconstruction time by our two-orbit 3D-OSEM was greatly reduced by parallelization with PC cluster, and compared with Feldkamp-FBP, the computation time was about 7 min longer with the PC cluster whereas it was about 52 min longer with the single PC.

As shown in Fig. 6, the image reconstructed by the cluster with six PCs was virtually identical with that with the single PC, and considerably better than image by the single-orbit Feldkamp-FBP method. The reconstruction error ε for the difference between these two images was 0.0001% from Eq. 2.

Discussion

We recently demonstrated that the major limitations in conventional pinhole SPECT, namely, non-uniform spatial resolution or axial blurring in reconstruction images were dramatically improved by complete data acquired using two circular orbits, combined with 3D-OSEM iterative reconstruction. One of the drawbacks of this approach is that it takes a long time to reconstruct in compensation for excellent image from two

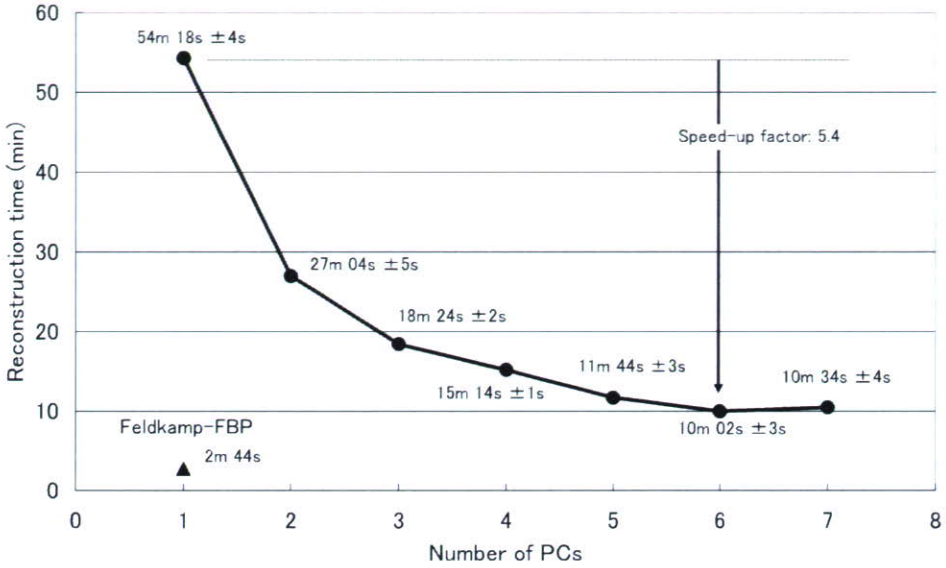

Fig. 5 Relationship between the number of PCs and reconstruction time (min) in parallel computing using the PC cluster

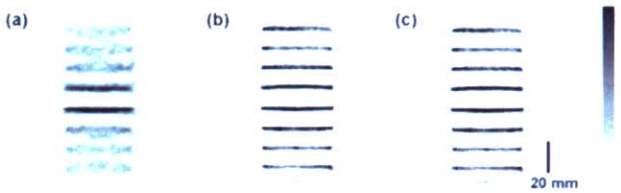

Fig. 6 Coronal images of the multiple-disk phantom reconstructed. The image (**a**) was reconstructed by the single-orbit Feldkamp-filtered back-projection method on single PC. The image (**b**) was reconstructed by the two-orbit 3D-OSEM method on single PC. The image (**c**) was reconstructed by the two-orbit 3D-OSEM method with PC cluster (six PCs)

independent projection data sets with two circular orbits. In this study, the long reconstruction time could be markedly reduced by parallel computing with the PC cluster. The parallelized reconstruction could be needed when resolution recovery, attenuation correction, and scatter correction are used in pinhole SPECT because they also increase the computation time [22].

The image reconstructed using the PC cluster was compared with that using the single PC. The error ε for evaluating the difference between these two images was 0.0001%, meaning that they were virtually identical. This slight error is attributed to the fact that the order of the addition of data back-projected from each view in the PC cluster is different from that in the single PC, and might have occurred during computation of the partial back-projection. However, this difference is negligible as shown by the small value of ε.

In this study, the reconstruction time with seven PCs was not improved compared with that with six PCs, as shown in Fig. 5, because the number of projections processed per one PC in the case of both six and seven PCs were equal. The partial back-projected images on each PC have to be transferred to all PCs, to sum those images on all PCs as shown in Process 2 in Fig. 3. Therefore, the communication time using seven PCs was longer than that using six PCs. The network performance is important for the Beowulf PC cluster.

This study was performed using the cluster with seven PCs. If the cluster had 30 PCs, one PC would process for only one projection. Assuming a linear model and roughly estimating from the results of this study, the reconstruction time using 30 PCs will equal that of 2–3 min with single-orbit FBP. Practically linear speed-up is not expected because back-projection is not a complete parallel process. The partial back-projected images on all PCs have to be transferred to all PCs and then summed on each PC with synchronization. We should consider that the communication time to transfer the partial images increases with increasing the number of PCs or enlarging the size of data. A high-performance communication network is essential for such cases [19]. When the size of the data is large, sufficient physical memory should be prepared to avoid memory swapping which increases the computation time.

To further improve the PC cluster, we must consider optimizing the use of each PC. In this study, there is an imbalance of the load distribution when using seven PCs. As shown in Table 2, while PC 1 and PC 2 process

for the fifth projections of the projections distributed, the other PCs are idle. If projections processed are more evenly distributed to all PCs, the speed of computation should be improved further. The reason for such a non-uniform distribution in this system is that one detector space cannot be decomposited in the combination of voxel-driven projector and PSD. There are two approaches available to evenly distribute data for all the PCs: (i) apply a ray-driven projector [23] instead of voxel-driven one for PSD because it allows the decomposition of one detector space and (ii) apply the image space decomposition method [18] for voxel-driven projector. However, further investigations are required to confirm that these alternative approaches improve the computation speed. When the cluster has slow PCs or other tasks use the resources in the cluster, the reconstruction time will increase as a result of spending too much time on slow PCs. In the present system, the fast PCs wait until the slow PCs complete the back-projection process. If the cluster system monitors the computation speed and the progress of the process on each PC and manages the distribution of the process to idle or fast PCs, the speed-down of reconstruction will be avoided [16].

At present we do not parallelize for one PC with multiple processors. Because the multiple processors on one PC can share memory, communication through the network for summing partial images is unnecessary [16]. Shattuck et al. [17] reported that a four-processor computer was able to achieve speed-up factors of approximately 3.4 relative to a single processor. Parallelization for both cluster PCs and multiple processors will effectively speed up the reconstruction time.

The Beowulf PC cluster system can be constructed using essentially free-software such as Linux operating system and MPI, and inexpensive PCs instead of super computer. Also, modifications of only approximately 10 lines were required to parallelize the reconstruction program. Although this article describes parallelization for the two-orbit pinhole SPECT, the strategy can be generalized for any pinhole SPECT (e.g., single orbit, helical orbit, and multipinholes).

Conclusions

We were able to markedly improve the long computation time of 3D-OSEM reconstruction in two-circular orbit pinhole SPECT by parallel computing using the PC cluster. The reconstruction time of 54 min decreased to 10 min by using six PCs. The speed-up factor was 5.4. The PC cluster is effective in decreasing the computing time with low cost and easy construction.

Acknowledgment This study was partly supported by the Japan Science and Technology Agency (JST).

References

1. Jaszczak RJ, Li J, Wang H, Zalutsky MR, Coleman RE. Pinhole collimation for ultra-high-resolution, small-field-of-view SPECT. Phys Med Biol 1994;39:425–37.
2. Weber DA, Ivanovic M, Franceschi D, Strand SE, Erlandsson K, Franceschi M, et al. Pinhole SPECT: an approach to in vivo high resolution SPECT imaging in small laboratory animals. J Nucl Med 1994;35:342–8.
3. Ishizu K, Mukai T, Yonekura Y, Pagani M, Fujita T, Magata Y, et al. Ultra-high resolution SPECT system using four pinhole collimators for small animal studies. J Nucl Med 1995;36:2282–7.
4. Ogawa K, Kawade T, Nakamura K, Kubo A, Ichihara T. Ultra high resolution pinhole SPECT for small animal study. IEEE Trans Nucl Sci 1998;45:3122–6.
5. Hirai T, Nohara R, Ogoh S, Chen LG, Kataoka K, Li XH, et al. Serial evaluation of fatty acid metabolism in rats with myocardial infarction by pinhole SPECT. J Nucl Cardiol 2001;8:472–81.
6. Scherfler C, Donnemiller E, Schocke M, Dierkes K, Decristoforo C, Oberladstätter M, et al. Evaluation of striatal dopamine transporter function in rats by in vivo β-[^{123}I]CIT pinhole SPECT. Neuroimage 2002;17:128–41.
7. Acton PD, Choi SR, Plössl K, Kung HF. Quantification of dopamine transporters in the mouse brain using ultra-high resolution single-photon emission tomography. Eur J Nucl Med 2002;29:691–8.
8. Aoi T, Watabe H, Deloar HM, Ogawa M, Teramoto N, Kudomi N, et al. Absolute quantitation of regional myocardial blood flow of rats using dynamic pinhole SPECT. In: Conference Record of 2002 IEEE Nuclear Science Symposium and Medical Imaging Conference (CD-ROM), 2003. p. 1780–3.
9. Vanhove C, Defrise M, Franken PR, Everaert H, Deconinck F, Bossuyt A. Interest of the ordered subsets expectation maximization (OS-EM) algorithm in pinhole single-photon emission tomography reconstruction: a phantom study. Eur J Nucl Med 2000;27:140–6.
10. Shepp LA, Vardi Y. Maximum likelihood reconstruction for emission tomography. IEEE Trans Med Imag 1982;MI-1:113–22.
11. Hudson HM, Larkin RS. Accelerated image reconstruction using ordered subsets of projection data. IEEE Trans Med Imag 1994;13:601–9.
12. Feldkamp LA, Davis LC, Kress JW. Practical cone-beam algorithm. J Opt Soc Am A 1984;1:612–9.
13. Zeniya T, Watabe H, Aoi T, Kim KM, Teramoto N, Hayashi T, et al. A new reconstruction strategy for image improvement in pinhole SPECT. Eur J Nucl Med Mol Imaging 2004;31:1166–72.
14. Aoi T, Zeniya T, Watabe H, Deloar HM, Matsuda T, Iida H. System design and development of a pinhole SPECT system for quantitative functional imaging of small animals. Ann Nucl Med 2006;20:245–51.
15. Tuy HK. An inversion formula for cone-beam reconstruction. SIAM J Appl Math 1983;43:546–52.
16. Vollmar S, Michel C, Treffert JT, Newport DF, Casey M, Knöss C, et al. *HeinzelCluster*: accelerated reconstruction for FORE and OSEM3D. Phys Med Biol 2002;47:2651–8.

17. Shattuck DW, Rapela J, Asma E, Chatzioannou A, Qi J, Leahy RM. Internet2-based 3D PET image reconstruction using a PC cluster. Phys Med Biol 2002;47:2785–95.
18. Jones JP, Jones WF, Kehren F, Newport DF, Reed JH, Lenox MW, et al. SPMD cluster-based parallel 3-D OSEM. IEEE Trans Nucl Sci 2003;50:1498–502.
19. Jones JP, Jones WF, Everman J, Panin V, Michel C, Kehren F, et al. Impact of a high-performance communication network on cluster-based parallel iterative reconstruction. In: Conference Record of 2005 IEEE Nuclear Science Symposium and Medical Imaging Conference (CD-ROM), 2006. p. 2273–7.
20. Rong Z, Tianyu M, Yongjie J. Parallel OSEM reconstruction algorithm for fully 3-D SPECT on a Beowulf cluster. Conf Proc IEEE Eng Med Biol Soc 2005;2:1834–7.
21. Watabe H, Woo SK, Kim KM, Kudomi N, Iida H. Performance improvement of event-based motion correction for PET using a PC cluster. In: Conference Record of 2003 IEEE Nuclear Science Symposium and Medical Imaging Conference (CD-ROM), 2004. p. 2407–9.
22. Sohlberg A, Watabe H, Zeniya T, Iida H. Comparison of multi-ray and point-spread function based resolution recovery methods in pinhole SPECT reconstruction. Nucl Med Commun 2006;27:823–7.
23. Sohlberg A, Ruotsalainen U, Watabe H, Iida H, Kuikka JT. Accelerated median root prior reconstruction for pinhole single-photon emission tomography (SPET). Phys Med Biol 2003;48:1957–69.

IOP PUBLISHING PHYSICS IN MEDICINE AND BIOLOGY
Phys. Med. Biol. 52 (2007) 1893–1908 doi:10.1088/0031-9155/52/7/009

Separation of input function for rapid measurement of quantitative $CMRO_2$ and CBF in a single PET scan with a dual tracer administration method

Nobuyuki Kudomi, Hiroshi Watabe, Takuya Hayashi and Hidehiro Iida

Department of Investigative Radiology, Advanced Medical-Engineering Center, National Cardiovascular Center-Research Institute, 5-7-1, Fujishirodai, Suita, Osaka 565-8565, Japan

E-mail: kudomi@ri.ncvc.go.jp

Received 1 September 2006, in final form 3 January 2007
Published 12 March 2007
Online at stacks.iop.org/PMB/52/1893

Abstract

Cerebral metabolic rate of oxygen ($CMRO_2$), oxygen extraction fraction (OEF) and cerebral blood flow (CBF) images can be quantified using positron emission tomography (PET) by administrating ^{15}O-labelled water ($H_2^{15}O$) and oxygen ($^{15}O_2$). Conventionally, those images are measured with separate scans for three tracers $C^{15}O$ for CBV, $H_2^{15}O$ for CBF and $^{15}O_2$ for $CMRO_2$, and there are additional waiting times between the scans in order to minimize the influence of the radioactivity from the previous tracers, which results in a relatively long study period. We have proposed a dual tracer autoradiographic (DARG) approach (Kudomi *et al* 2005), which enabled us to measure CBF, OEF and $CMRO_2$ rapidly by sequentially administrating $H_2^{15}O$ and $^{15}O_2$ within a short time. Because quantitative CBF and $CMRO_2$ values are sensitive to arterial input function, it is necessary to obtain accurate input function and a drawback of this approach is to require separation of the measured arterial blood time–activity curve (TAC) into pure water and oxygen input functions under the existence of residual radioactivity from the first injected tracer. For this separation, frequent manual sampling was required. The present paper describes two calculation methods: namely a linear and a model-based method, to separate the measured arterial TAC into its water and oxygen components. In order to validate these methods, we first generated a blood TAC for the DARG approach by combining the water and oxygen input functions obtained in a series of PET studies on normal human subjects. The combined data were then separated into water and oxygen components by the present methods. CBF and $CMRO_2$ were calculated using those separated input functions and tissue TAC. The quantitative accuracy in the CBF and $CMRO_2$ values by the DARG approach did not exceed the acceptable range, i.e., errors in those values were within 5%, when the area under the curve in the input function of the second tracer was larger than half of the first one. Bias and deviation in those values were also compatible to that of the conventional method, when noise

was imposed on the arterial TAC. We concluded that the present calculation based methods could be of use for quantitatively calculating CBF and $CMRO_2$ with the DARG approach.

1. Introduction

Cerebral metabolic rate of oxygen ($CMRO_2$), oxygen extraction fraction (OEF) and cerebral blood flow (CBF) images have enabled us to understand the pathophysiological basis of cerebrovascular disorders. Positron emission tomography (PET) allows us to quantitatively measure the CBF and $CMRO_2$. These measurements can be achieved using a protocol involving separate PET scans, one after the administration of each of three distinct ^{15}O-labelled radioactive tracers: $H_2{}^{15}O$ or $C^{15}O_2$ for CBF, $^{15}O_2$ for $CMRO_2$, and $C^{15}O$ for cerebral blood volume (CBV) (Frackowiack *et al* 1980a, 1980b, Mintun *et al* 1984, Lammertsma and Jones 1983). However, the complex procedure and its relatively long protocol often limit its applicability and also make it difficult to perform at different physiological conditions.

Quantitative images of CBF and $CMRO_2$ by PET are calculated on the basis of a single-tissue compartment model of oxygen and water kinetics (Frackowiack *et al* 1980a, 1980b, Mintun *et al* 1984, Lammertsma and Jones 1983). The steady-state method (Subramanyam *et al* 1978, Lammertsma *et al* 1982, Correia *et al* 1985, Okazawa *et al* 2001a, 2001b) has been employed in a number of studies in which quantitative images are estimated from data acquired while in the steady state reached during continuous inhalation of $C^{15}O_2$ and $^{15}O_2$. This method can be employed using a simple procedure and mathematical formula, but has several limitations. A prolonged data-acquisition period (approximately 1 h) is required, and the procedure is sensitive to error sources such as statistical noise and tissue heterogeneity (Lammertsma *et al* 1982, Correia *et al* 1985). An additional drawback is the relatively high level of radiation exposure required to reach the steady state.

An alternative autoradiographic method (ARG) using only short administration times for each of the three tracers, i.e., the three-step autoradiographic method (3SARG) has been developed (Mintun *et al* 1984) and subsequently simplified and optimized (Iida *et al* 1993, Sadato *et al* 1993, Hatazawa *et al* 1995, Shidahara *et al* 2002, Hattori *et al* 2004). CBF images can be obtained by a $H_2{}^{15}O$ autoradiographic method, using a PET counts-versus-CBF nomogram, which follows a simple look-up table procedure (Raichle *et al* 1983, Herscovich *et al* 1983, Kanno *et al* 1987); the quantitative accuracy of these images is improved when influence of input delay, which is the time difference between brain input function and detector device, and dispersion, which is caused by flow speed difference of liquid in a catheter tube due to viscosity, are corrected (Iida *et al* 1986, 1988). $CMRO_2$ and the oxygen extraction fraction (OEF) can be estimated using data acquired during $^{15}O_2$ inhalation, but must be corrected for clearance of radioactivity associated with CBF (Mintun *et al* 1984), CBV and the level of recirculating radioactive water (Iida *et al* 1993). Although the total time required for 3SARG is less than that of the steady-state method, it still requires at least half an hour, with waiting times between the scans to reduce the radioactivity of the tracer administered previously.

There have been other attempts to obtain CBF and $CMRO_2$ images more rapidly (Huang *et al* 1986, Holden *et al* 1988, Meyer *et al* 1987, Ohta *et al* 1992, Ho and Feng 1999). Mathematical refinement has allowed images to be generated from data from a single scan alone upon a bolus inhalation of $^{15}O_2$. The quality of the image suffers, however, from statistical noise due to the lack of predictability of the multiple parameters of CBF, $CMRO_2$, and the arterial vascular compartment (V_0) and the limited acquisition time (Meyer *et al* 1987, Ohta *et al* 1992). Therefore, this technique has not been generally applied in clinical settings,

but has been used primarily for research purposes (Fujita *et al* 1999, Vafaee and Gjedde 2000, Okazawa *et al* 2001a, 2001b, Mintun *et al* 2002).

Recently, rapid CBF and $CMRO_2$ measurement was achieved by administration of dual tracers during a single PET scan and the use of an integration method, i.e., dual tracer autoradiographic (DARG) approach (Kudomi *et al* 2005). This approach can shorten the total study period for both CBF and $CMRO_2$ measurement as compared to the 3SARG approach. It is thus expected to serve as a tool for faster or repeated assessment of flow and metabolism during multiple physiological or pathological conditions while maintaining the image quality and quantitative accuracy.

The DARG protocol was typically implemented in a short time interval of 3 min in a single PET scan conducted during the sequential administration of $H_2^{15}O$ and $^{15}O_2$. A mathematical formula based on the integration method was derived to calculate the values of CBF, OEF and $CMRO_2$ from the PET scan data, and was applicable to the data obtained after the administration of tracers in either order, i.e. $H_2^{15}O$ injection followed by $^{15}O_2$ inhalation ($H_2^{15}O$–$^{15}O_2$) or $^{15}O_2$ inhalation followed by $H_2^{15}O$ injection ($^{15}O_2$–$H_2^{15}O$). In the formula, the radioactivity concentrations in the artery, i.e. arterial input functions for the ^{15}O-labelled oxygen and ^{15}O-labelled water must be provided in order to compute the quantitative CBF and $CMRO_2$ values.

The arterial input function of whole blood including oxygen and water is usually obtained from a continuously measured arterial blood time–activity curve (TAC) by a beta-ray detector (Kanno *et al* 1987, Iida *et al* 1986) or coincidence detector (Eriksson *et al* 1988, Eriksson and Kanno 1991, Votaw *et al* 1998, Kudomi *et al* 2003). In the DARG approach, it is necessary to separate the $^{15}O_2$ and $H_2^{15}O$ contents in the arterial TAC during the second phase of the scan because the arterial blood contains not only the radioactivity of the second tracer but also the residual activity of the first tracer. Thus, the radioactivity in the arterial blood during the second phase of the scan is always the summation of the radioactivity from $^{15}O_2$ and $H_2^{15}O$. Moreover, after its administration, $^{15}O_2$ coexists in arterial blood with labelled or recirculating $H_2^{15}O$, which is a metabolite. A modelling approach (Iida *et al* 1993) enables us to predict the TAC of the recirculating water, but this approach is based on an assumption that there is no radioactivity in the arterial blood at the time of $^{15}O_2$ administration and it cannot be applied when residual radioactivity of $H_2^{15}O$ exists in the arterial blood. Instead of using the modelling approach, Kudomi *et al* (2005) performed frequent manual sampling of arterial blood and centrifugation to separate plasma from whole blood in order to predict the recirculating water content in the whole blood. However, this procedure is labour intensive and hampers the clinical application of the DARG protocol.

In this paper, we have proposed two methods: (A) a linear method and (B) a model-based method to separate the $^{15}O_2$ and $H_2^{15}O$ contents from a measured arterial TAC in which both $^{15}O_2$ and $H_2^{15}O$ coexisted for the DARG approach. By these methods, no manual sampling of arterial blood is required to separate the $^{15}O_2$ and $H_2^{15}O$ contents. In order to evaluate the proposed methods, simulation studies were performed.

2. Materials and methods

2.1. Separation methods

In this section, we described two separation methods. In both methods, the separation procedure from measured whole blood TAC ($A_t(t)$) to input functions of pure $H_2^{15}O$ ($F_w(t)$) and $^{15}O_2$ ($F_o(t)$) consists of two parts, one is to account for residual activity for the first tracer

during the second phase, and the other is to account for the metabolic product of $^{15}O_2$, i.e., recirculating water.

(A) Linear method. For the $H_2^{15}O$–$^{15}O_2$ protocol, we first estimated the TAC for the residual radioactivity from the first tracer ($H_2^{15}O$) remaining during the second phase by extrapolating the combined TAC in the first phase by the following linear function:

$$F_L(t) = at + b \tag{1}$$

where t is the time and a and b are the parameters being estimated. We then subtracted the fitting function equation (1) from the measured TAC in the second phase, and obtained first ($F_1(t)$) and second tracer TAC ($F_2(t)$) as

$$\begin{aligned} F_1 &= A_t(t) \quad (t < t_{2nd}) \\ &= F_L(t) \quad (t > t_{2nd}) \end{aligned} \tag{2}$$

$$\begin{aligned} F_2 &= 0 \ (t < t_{2nd}) \\ &= A_t(t) - F_L(t) \quad (t > t_{2nd}) \end{aligned} \tag{3}$$

where t_{2nd} is the time of second tracer administration. Second, the TAC of the metabolic product (recirculating water) ($F_{rw}(t)$) following $^{15}O_2$ administration was estimated in the second phase, using the modelling approach described previously (Iida *et al* 1993). The model proposed the assumption of a fixed rate constant ($k = 0.0722\ min^{-1}$) for production of recirculating water, and predicted the appearance of the recirculating water from the measured whole blood TAC as

$$F_{rw}(t) = kF_2(t - \Delta t) \otimes e^{-kt} \tag{4}$$

where Δt indicates the delay time of appearance of recirculating water and $\otimes$ denotes the convolution integral. Finally, the TAC of the recirculating water (equation (4)) was added to $F_1(t)$ to obtain a TAC for $H_2^{15}O$ ($F_w(t)$), and also subtracted from $F_2(t)$ to obtain a pure TAC for $^{15}O_2$ ($F_o(t)$), i.e.,

$$\begin{aligned} F_w &= A_t(t) \quad (t < t_{2nd}) \\ &= F_L(t) + F_{rw}(t) \quad (t > t_{2nd}) \end{aligned} \tag{5}$$

$$\begin{aligned} F_o &= 0 \ (t < t_{2nd}) \\ &= A_t(t) - F_L(t) - F_{rw}(t) \quad (t > t_{2nd}). \end{aligned} \tag{6}$$

For the $^{15}O_2$–$H_2^{15}O$ protocol, we first obtained the TAC for the recirculating water due to the metabolism of oxygen during the first phase of $^{15}O_2$ administration using the modelling approach (Iida *et al* 1993) as

$$F_{rw}(t) = kA_t(t - \Delta t) \otimes e^{-kt} \quad (t < t_{2nd}) \tag{7}$$

and then separated the whole blood TAC into pure TACs for $^{15}O_2$ and $H_2^{15}O$ during the first phase. Second, we estimated the TAC for the residual radioactivity of $^{15}O_2$ during the second phase by extrapolating the estimated arterial $^{15}O_2$ TAC from the first phase by a linear function as in the case of the $H_2^{15}O$–$^{15}O_2$ protocol and then obtained pure TAC for $H_2^{15}O$ and $^{15}O_2$, i.e.,

$$\begin{aligned} F_w &= F_{rw}(t) \qquad (t < t_{2nd}) \\ &= A_t(t) - F_L(t) \quad (t > t_{2nd}) \end{aligned} \tag{8}$$

$$\begin{aligned} F_o &= A_t(t) - F_{rw}(t) \quad (t < t_{2nd}) \\ &= F_L(t) \qquad (t > t_{2nd}) \end{aligned} \tag{9}$$

where if $F_L(t)$ was less than 0, its value was set to zero.

(B) Model-based method. The input function after the injection of $H_2^{15}O$ was assumed to be the sum of two exponentials that were convolved with a Gauss function:

$$F'_w(t) = w_1 \exp(-w_3 t) \otimes g(w_5 t) + w_2 \exp(-w_4 t) \otimes g(w_6 t) \tag{10}$$

where F'_w represents the blood TAC for water administration but does not include the recirculating water from $^{15}O_2$ administration and $g(x)$ is a Gauss function as

$$g(px) = \exp(-p^2 x^2) \tag{11}$$

w_i (i = 1–6) are the parameters estimated.

The administration of $^{15}O_2$ is usually performed by the continuous inhalation of $^{15}O_2$ gas. The input function after the inhalation of $^{15}O_2$ was modelled using a rectangular function (f_{rect}) as follows:

$$F'_o(t) = f_{rect}(t) \otimes [o_1 \exp(-o_3 t) \otimes g(o_5 t) + o_2 \exp(-o_4 t) \otimes g(o_6 t)] \tag{12}$$

where F'_o represents the sum of the TAC of pure $^{15}O_2$ and recirculating water, and o_i (i = 1–6) are the parameters to be estimated. f_{rect} is defined as

$$\begin{aligned} f_{rect}(t) &= \text{constant} \quad (T_1 < t < T_2) \\ f_{rect}(t) &= 0 \qquad\quad (t < T_1 \text{ or } t > T_2) \end{aligned} \tag{13}$$

where $T_1 < t < T_2$ corresponds to the period of tracer administration.

The model function for the combined input function (F_t), i.e., whole blood TAC, is expressed by summing $F'_w(t)$ (equation (10)) and $F'_o(t)$ (equation (12)) as follows:

$$F_t(t) = F'_w(t - T_w) + F'_o(t - T_o) \tag{14}$$

where T_w and T_o denote the start time of $H_2^{15}O$ and $^{15}O_2$ administration, respectively. In our PET study, the interval between the injections of the two tracers was 180 s; therefore $T_w = 0$ and $T_o = 180$ s for the $H_2^{15}O$–$^{15}O_2$ protocol and $T_w = 180$ and $T_o = 0$ s for the $^{15}O_2$–$H_2^{15}O$ protocol.

The measured blood TAC was fitted for the whole period using the model function $F_t(t)$ in equation (14) by the variable-metric method (pseudo-Gauss–Newton method), and F'_w and F'_o were then obtained as the separated input functions. All computations, including the fitting operation, were carried out in the PAW environment (http://wwwasd.web.cern.ch/wwwasd/paw/). Finally, the TAC for recirculating water was obtained by applying the modelling approach (Iida *et al* 1993) using the obtained $F'_o(t)$ as

$$F_{rw}(t) = k F'_o(t - \Delta t) \otimes e^{-kt} \tag{15}$$

and the estimated recirculating water TAC was added to $F'_w(t)$ and subtracted from the obtained $F'_o(t)$, which resulted in the pure TACs of $H_2^{15}O$ and $^{15}O_2$, i.e.,

$$\begin{aligned} F_w(t) &= F'_w(t) + F_{rw}(t) \\ F_o(t) &= F'_o(t) - F_{rw}(t). \end{aligned} \tag{16}$$

2.2. *Simulation studies*

The reliability of the present methods was tested using actual blood TACs obtained in a series of PET studies.

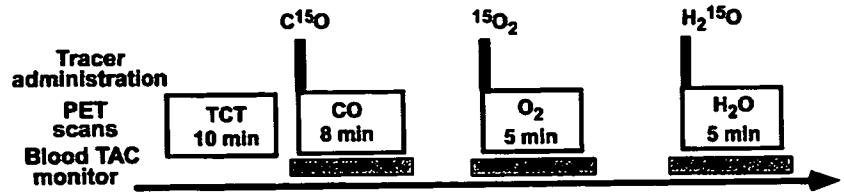

Figure 1. PET study protocol on normal human subjects. After a 10 min transmission scan and $C^{15}O$ (3000 MBq) emission scan, gaseous $^{15}O_2$ (3000 MBq) was inhaled for 1 min and a scan for 5 min was started at the same time. After sufficient time for radioactive decay of $^{15}O_2$, a $H_2^{15}O$ PET scan for 5 min was started with an intravenous administration of $H_2^{15}O$ (1110 MBq). The concentration of the radioactivity in the arterial blood was monitored (blood TAC monitor) continuously by a beta-ray detector, started at 30 s before and stopped at 30 s after the PET scan.

2.2.1. PET studies. A series of PET scans to measure the CBF and $CMRO_2$ were carried out on ten normal human subjects. All subjects were males ($n = 10$, age $= 24.6 \pm 3.3$ years, body weight $= 65.6 \pm 9.0$ kg), who provided written informed consent. The PET procedures were approved by the ethical committee of the National Cardiovascular Center. The details of the PET procedure have been described previously (Shidahara *et al* 2002). The PET scanner used was an ECAT EXACT 47 (CTI Inc., Knoxville, USA). After a 10 min transmission scan and emission scan with the administration of 3000 MBq of $C^{15}O$ for 8 min, gaseous $^{15}O_2$ of 3000 MBq was inhaled for 1 min, and a dynamic scan for 5 min was started at the same time as the inhalation. After allowing sufficient time for radioactive decay of $^{15}O_2$, another scan for 5 min was initiated with an intravenous administration of $H_2^{15}O$ into the right brachial vein. The dose was approximately 1110 MBq and the infusion period was 10 s. The study protocol is shown in figure 1.

The concentration of the radioactivity in the arterial blood was monitored continuously by means of a beta-ray detector (Kanno *et al* 1987, Iida *et al* 1986) during the PET scan. A catheter was inserted into the brachial artery, and blood was withdrawn at a flow rate of 4 ml min^{-1}. The inner diameter of the tube was approximately 1.3 mm, and the distance from the catheter to the detector was 20–25 cm. Continuous blood sampling was started at 30 s before the start of the PET scan and stopped at 30 s after the end of the scan. For each PET study, the beta-ray detector was calibrated against a NaI(Tl) well counter which was cross calibrated to the PET scanner. The calibration was carried out using $H_2^{15}O$ filled in the tube. The cross calibration factor of the detector against the well counter was from 50 to 100 cps g^{-1} cps^{-1}.

2.2.2. Simulated input function for DARG protocol and separation. Combined input function (CIF) as a simulated input function was generated by combining the experimentally obtained input functions for $H_2^{15}O$ and $^{15}O_2$ administration. Ten sets of $H_2^{15}O$ and $^{15}O_2$ arterial TACs obtained in the series of PET studies were used to generate the CIF.

It is known that the measured arterial TAC is more dispersed and delayed relative to the true input TAC in the brain, due to transverses of blood in peripheral artery and catheter tube before reaching the detector (Iida *et al* 1986, 1988, 1989, 2000, Lammertsma *et al* 1990), those terms in blood TAC were corrected. Dispersion correction (Iida *et al* 1986) was applied to the arterial blood TACs with $H_2^{15}O$ and $^{15}O_2$. Also, delay was corrected for the $H_2^{15}O$ arterial TAC (Iida *et al* 1988, Shidahara *et al* 2002) and that for $^{15}O_2$ administration was corrected by applying the same time as for $H_2^{15}O$ for the same subject. For the arterial blood TAC with $^{15}O_2$, the recirculating water was estimated using the conventional modelling approach using

equation (7) (Iida *et al* 1993). Then, sets of two input functions for pure $^{15}O_2$ and $H_2^{15}O$ were obtained, which were denoted as true input functions (TIFs). Those two blood TACs for $H_2^{15}O$ and $^{15}O_2$ were added with a time lag of 180 s of the order of $H_2^{15}O$ and $^{15}O_2$ and reverse for the $H_2^{15}O$–$^{15}O_2$ and $^{15}O_2$–$H_2^{15}O$ protocols, respectively, and the CIFs were obtained. Note that two blood TACs without the correction for the physical decay of ^{15}O were used prior to combining, and the combined curve was corrected for the physical decay of ^{15}O.

Methods (A) and (B) were applied to the CIFs to separate the $^{15}O_2$ and $H_2^{15}O$ contents. For method (A), the fitting period was selected from 80, 100, 120, 140 and 160 s to 180 s.

2.2.3. Computation of functional values. Values of CBF, OEF and $CMRO_2$ were calculated from tissue TAC ($C_i(t)$) and separated input functions for $H_2^{15}O$ ($F_w(t)$) and for $^{15}O_2$ ($F_o(t)$) using mathematical formulae, based on a single-tissue compartment model for water and oxygen (Mintun *et al* 1984). The formulae were designed to be applicable to data for tracer administration in either order $H_2^{15}O$–$^{15}O_2$ or $^{15}O_2$–$H_2^{15}O$. The total radioactivity in the tissue after $^{15}O_2$ and $H_2^{15}O$ administration can be expressed as,

$$C_i(t) = f \cdot F_w \otimes e^{\frac{-f \cdot t}{p}} + E \cdot f \cdot F_o \otimes e^{\frac{-f \cdot t}{p}} + V_B \cdot R_{Hct}(1 - F_v \cdot E)F_o(t) \tag{17}$$

where f is CBF, E is the OEF, p is a blood/brain partition coefficient for water, V_B is cerebral blood volume, R_{Hct} is the small-to-large vessel haematocrit ratio and F_v is the effective venous fraction. The first term on the right-hand side describes the amount of water entering the tissue. The second represents the amount of oxygen that enters the tissue and is immediately metabolized to water. The third expresses the radioactivity of $^{15}O_2$ in blood vessels. In the present study, we assumed that the radioactivity of $H_2^{15}O$ in the blood vessel term is negligibly small compared to the radioactivity in tissue according to the previous study (Iida *et al* 2000).

To calculate functional values using a look-up table procedure, equation (17) was integrated for the periods after $H_2^{15}O$ ($\int_w$: integrate for 90 s after rise up of $H_2^{15}O$ tissue TAC) and $^{15}O_2$ administration ($\int_o$: integrate for 180 s after rise up of $^{15}O_2$ tissue TAC) as

$$\int_w C_i(t)\,dt = \int_w (f \cdot F_w \otimes e^{\frac{-f \cdot t}{p}} + E \cdot f \cdot F_o \otimes e^{\frac{-f \cdot t}{p}} + V_B \cdot R_{Hct}(1 - F_v \cdot E)F_o(t))\,dt \tag{18}$$

$$\int_o C_i(t)\,dt = \int_o (f \cdot F_w \otimes e^{\frac{-f \cdot t}{p}} + E \cdot f \cdot F_o \otimes e^{\frac{-f \cdot t}{p}} + V_B \cdot R_{Hct}(1 - F_v \cdot E)F_o(t))\,dt. \tag{19}$$

Equation (19) can be rewritten as

$$E = \frac{\int_o (C_i(t)\,dt - f \cdot F_w \otimes e^{\frac{-f \cdot t}{p}} - V_B \cdot R_{Hct} \cdot F_o(t))\,dt}{\int_o (E \cdot f \cdot F_o \otimes e^{\frac{-f \cdot t}{p}} - V_B \cdot R_{Hct} \cdot F_v \cdot F_o(t))\,dt}. \tag{20}$$

Substituting equation (20) into (18), we obtain

$$\begin{aligned}\int_w C_i(t)\,dt = {} & \int_w (f \cdot F_w \otimes e^{\frac{-f \cdot t}{p}} + V_B \cdot R_{Hct} \cdot F_o(t))\,dt \\ & + \int_w (f \cdot F_o \otimes e^{\frac{-f \cdot t}{p}} - V_B \cdot R_{Hct} \cdot F_v \cdot F_o(t))\,dt \\ & \times \frac{\int_o (C_i(t)\,dt - f \cdot F_w \otimes e^{\frac{-f \cdot t}{p}} - V_B \cdot R_{Hct} \cdot F_o(t))\,dt}{\int_o (E \cdot f \cdot F_o \otimes e^{\frac{-f \cdot t}{p}} - V_B \cdot R_{Hct} \cdot F_v \cdot F_o(t))\,dt}.\end{aligned} \tag{21}$$

Using equation (21), f can be estimated using a look-up table procedure based on the tissue TAC and separated input functions. Next, E can be calculated using equation (20). $CMRO_2$ is

then calculated from the estimated f and E, and the measured arterial oxygen content ($[O_2]_a$) as $CMRO_2 = 1.36 \cdot [O_2]_a \cdot E \cdot f$.

2.2.4. Error analysis in the separation procedure. The error in the separation of the input function by the proposed methods propagates into the quantitative values of CBF and $CMRO_2$. This error propagation was investigated by the simulation study.

Ten sets of TIFs for $H_2^{15}O$ and $^{15}O_2$ were used to generate tissue TACs using equation (17). Two sets of physiological conditions were simulated, namely the normal condition (CBF = 50 ml/100 g min^{-1}, OEF = 0.4, CBV = 0.04 ml g^{-1}, $p = 0.8$ ml g^{-1}, $F_v = 0.835$, and $R_{Hct} = 0.85$) (Hayashi *et al* 2003) and ischaemic condition (CBF = 20 ml/100 g min^{-1}, OEF = 0.7, CBV = 0.04 ml g^{-1}, $p = 0.8$ ml g^{-1}, $F_v = 0.835$ and $R_{Hct} = 0.85$).

The combined tissue TACs for both orders of the DARG protocol, i.e. $H_2^{15}O$–$^{15}O_2$ and $^{15}O_2$–$H_2^{15}O$ were created by adding generated tissue TACs of $H_2^{15}O$ and $^{15}O_2$ with a 3 min time lag.

The values of CBF and $CMRO_2$ were calculated according to the formulae described above (equations (20) and (21)) using separated input functions from the CIF and the combined tissue TACs. The errors in the form of biases and deviations in estimated CBF and $CMRO_2$ values were calculated by comparing them with the assumed CBF and $CMRO_2$ values. These errors were presented as percentage differences between the calculated and assumed values.

2.2.5. Influence of dose of second tracer. In the DARG protocol, if administration dose of the second tracer is relatively smaller than that of the first tracer, the portion of the residual radioactivity from the first tracer in the second blood TAC becomes larger. Contrarily, if administration dose of the second tracer is larger than that of the first tracer, contribution of residual radioactivity from the first tracer on the second blood TAC becomes smaller. Therefore, errors of the separation methods and consequently the errors in the values of CBF and $CMRO_2$ might depend on the administration dose of the second tracer with respect to that of the first tracer.

We investigated how the error size would change when the second dose, i.e. the amount of the second input function, changed. For this purpose, the height of the oxygen input function in CIF was changed so that the ratio of the AUC (area under curve) between the $H_2^{15}O$ and $^{15}O_2$ input functions was changed stepwise from half to two-fold. The error size in the CBF and $CMRO_2$ values was analysed in the same way as above using separation methods (A) and (B).

2.2.6. Influence of noise in arterial TAC. The size of the error in the values of CBF and $CMRO_2$ might also depend on the statistical fluctuation in the arterial TAC, and we investigated the change in error size in the CBF and $CMRO_2$ values when the statistical fluctuations of the arterial TAC changed. To investigate the error size, 1000 noisy arterial TACs (noisy CIF) were created by adding Gaussian noise to the CIFs. The noise was added every second in a form given by $n(t) = \alpha \cdot G(\sqrt{C(t)})$. Here, $C(t)$ and $n(t)$ denote the arterial TAC count in a second without decay and noise correction at time t, respectively, and $G(\sigma)$ is the Gaussian noise with the standard deviation σ. The noise level α was defined so that the coefficient of variance in the water arterial TAC at its peak was set to 1, 2, 4, 8, 16 and 32%. The noisy arterial TACs were separated by methods (A) and (B). The values of CBF and $CMRO_2$ were then calculated using these separated TACs, and the errors in the form of biases and deviations in those values were presented as percentage differences from the assumed values. In addition, noise was also added to TIFs, and CBF, OEF and $CMRO_2$ were calculated to investigate how the noise in the

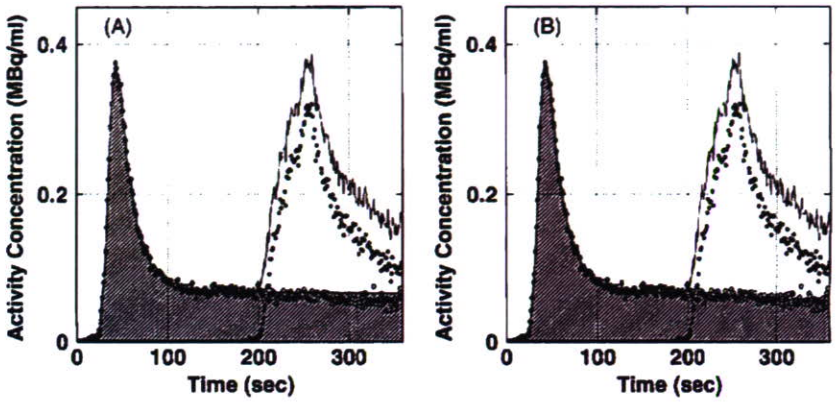

Figure 2. Estimated input function in the second phase (hatched region) from blood TAC (solid line) for DARG of $H_2^{15}O$–$^{15}O_2$. The blood TACs in which two components coexist were derived by combining two blood TACs of ^{15}O-water (white circles) and ^{15}O-oxygen (black circles) with a 180 s time lag. (A) Residual radioactivity of the first tracer was estimated by method (A) (fitting interval: 120 to 180 s). (B) Residual radioactivity of the first tracer was estimated by method (B).

arterial TAC without the separation procedure contributes to errors in the CBF, OEF and $CMRO_2$ values.

3. Results

Among ten normal subjects, the mean values of AUC for a period of 180 s for the arterial TAC were 80 ± 19 kBq ml^{-1} and 55 ± 10 kBq ml^{-1} for $H_2^{15}O$ and $^{15}O_2$, respectively. This result indicated that the values of AUC for $H_2^{15}O$ and $^{15}O_2$ had an ambiguity of approximately 20%, although all the subjects received the same amount of dose and processes for administration in the present PET study condition.

Figures 2 and 3 show examples of the separated input functions for the DARG protocols of $H_2^{15}O$–$^{15}O_2$ and $^{15}O_2$–$H_2^{15}O$ with the original and combined input functions using methods (A) and (B). It took about 40 s to separate the input function in method (B), and less than 1 s in method (A) (CPU: Intel® Pentium® D 3.2 GHz, memory: 1.0 GB, OS: Linux Fedora Core 4). For both methods and protocols, the estimated residual radioactivity in the second phase with respect to the first (hatched region) was almost identical to the true (original) input function (white circle).

For the linear method (A), the fitting interval from 120 to 180 s, where the slope of the input function became stable, provided the best fit for both the protocols, as shown in table 1. The table shows the fitting interval provided minimal bias and deviation in the difference of area under the curve between CIF and separated TAC for the residual tracer radioactivity in the second phase. When the start time of that interval was less than 120 s, the change in slope of the input function for the first tracer was large and the linear function could not reproduce the TAC of the residual radioactivity in the second phase. Further, when the time was greater, the amount of data was too inadequate to reproduce the TAC in the second phase.

Table 2 summarizes the error in the CBF and the $CMRO_2$ values due to the separation in input functions. The size of the bias and deviation in the CBF and the $CMRO_2$ values were within 4% for all separation procedures in both conditions.

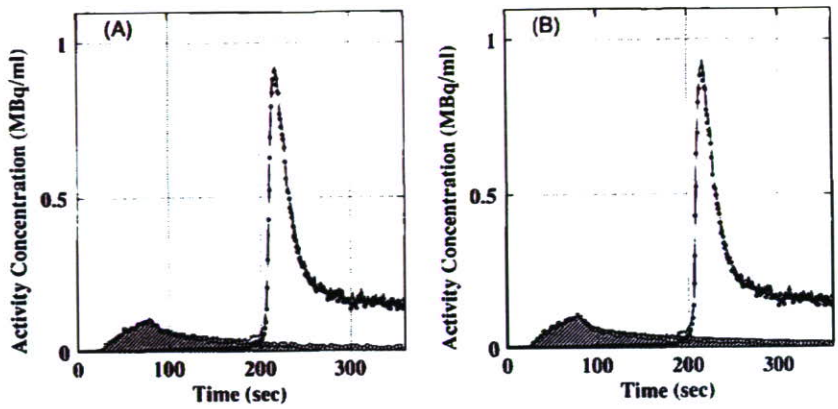

Figure 3. Estimated input function in the second phase (hatched region) from blood TAC (solid line) for DARG of $^{15}O_2$–$H_2^{15}O$. The blood TAC in which two components coexist was derived by combining two blood TACs of ^{15}O-oxygen (black circles) and ^{15}O-water (white circles) with a 180 s time lag. (A) Residual radioactivity of the first tracer was estimated by method (A) (fitting interval: 120 to 180 s) (B) Residual radioactivity of the first tracer was estimated by method (B).

Table 1. Bias and deviation in the difference of area under the curve between CIF and the estimated residual tracer radioactivity in the second phase by the linear method against the fitting interval ($n = 10$). Bias and deviation are given in %.

Fitting interval (s)	60–180	80–180	100–180	120–180	140–180	160–180
H_2O–O_2 protocol	106.9 ± 37.8	46.7 ± 44.3	10.5 ± 20.8	0.5 ± 14.5	−1.8 ± 17.2	25.4 ± 40.3
O_2–H_2O protocol	9.1 ± 5.6	8.7 ± 7.2	7.2 ± 6.6	5.3 ± 4.5	5.6 ± 7.2	7.7 ± 15.6

Table 2. Bias and deviation in CBF and $CMRO_2$ propagated from the error in the separation of $^{15}O_2$ and $H_2^{15}O$ input function ($n = 10$).

		Bias ± deviation (%)			
		Normal condition		Ischaemic condition	
Model function	Fitting interval (s)	CBF	$CMRO_2$	CBF	$CMRO_2$
$H_2^{15}O$–$^{15}O_2$					
(A)	120–180	–	−1.9 ± 4.2	–	−2.2 ± 3.5
(B)	0–360	–	0.4 ± 1.6	–	0.3 ± 1.9
$^{15}O_2$–$H_2^{15}O$					
(A)	120–180	−2.1 ± 1.2	1.3 ± 0.6	−1.7 ± 1.1	1.7 ± 0.6
(B)	0–360	−0.3 ± 1.4	0.2 ± 0.5	−0.2 ± 1.7	0.2 ± 0.1

Normal condition: CBF = 50 ml min^{-1}/100 g, OEF = 0.4; ischaemic condition: CBF = 20 ml min^{-1}/100 g, OEF = 0.7.

The bias and deviation in the value of CBF for $^{15}O_2$–$H_2^{15}O$ and $CMRO_2$ for both $H_2^{15}O$–$^{15}O_2$ and $^{15}O_2$–$H_2^{15}O$ are shown as functions of the ratio of AUC between the first and second input functions in figure 4. The size of the bias and deviation increased with the decrease in the second tracer dose and was suppressed since the second dose was increased in both methods (A) and (B). The size of the bias in the CBF by the $^{15}O_2$–$H_2^{15}O$ protocol and the $CMRO_2$ by the $H_2^{15}O$–$^{15}O_2$ protocol was 2% at most and was almost the same in the range of the AUC ratio from half to two-fold. The size of the bias in $CMRO_2$ by the $^{15}O_2$–$H_2^{15}O$ protocol was

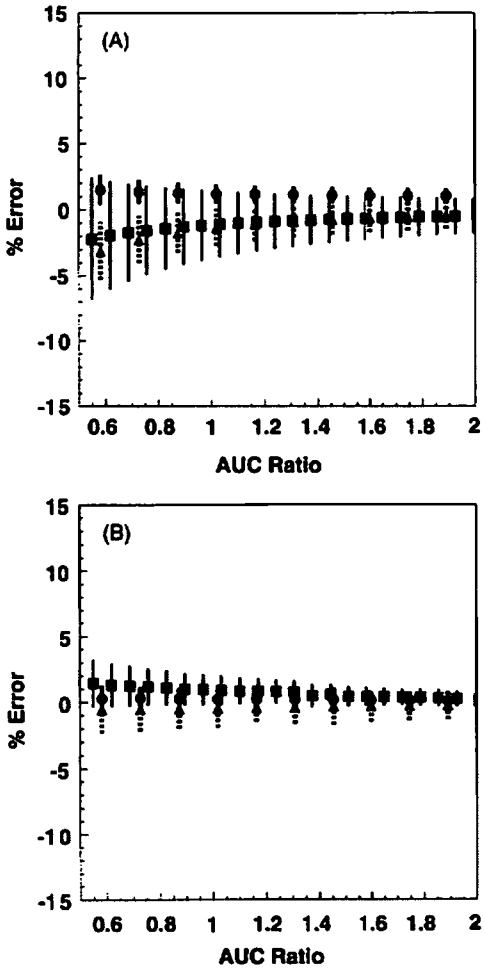

Figure 4. Error in CBF and $CMRO_2$ as a function of the dose ratio between the first to second tracer using separated input functions in method (A) (top) and (B) (bottom). The sizes of the bias in the values of CBF for $^{15}O_2$–$H_2^{15}O$ (circles) and $CMRO_2$ for $H_2^{15}O$–$^{15}O_2$ (squares) and $CMRO_2$ for $^{15}O_2$–$H_2^{15}O$ (triangles) are plotted and that of the deviation is expressed as the length of the bar.

almost negligible, and it was smaller than 0.5% in the same range of the AUC ratio. The size of the deviation for the CBF in the $^{15}O_2$–$H_2^{15}O$ protocol was less than 0.5%, and the sizes of the deviation for $CMRO_2$ in the $^{15}O_2$–$H_2^{15}O$ protocol and the $H_2^{15}O$–$^{15}O_2$ protocol were less than 3% and 4%, respectively.

The size of the bias and the deviation in the CBF, OEF and $CMRO_2$ values, due to the noise in the arterial TAC are shown in figure 5. The size of the bias for the separation method (B) (denoted by triangles) in those values was less than 5% when the noise level was less than 10%, and it was almost identical to that estimated using noisy TIF (denoted by circles). The bias by method (A) (denoted by squares) was larger than that by method (B). For the deviation with respect to the noise TIF, the size of the error in the CBF, OEF and $CMRO_2$ values was almost identical for both methods (A) and (B).

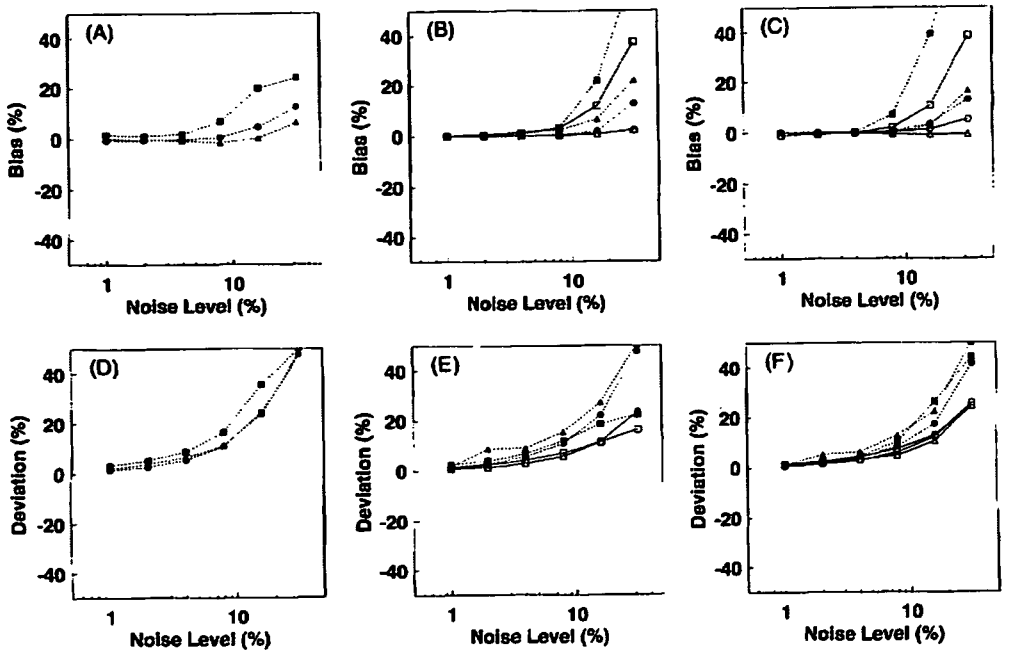

Figure 5. Bias (upper) and deviation (lower) against noise level in CBF (left), OEF (centre) and $CMRO_2$ (right) propagated from the noise on arterial TAC. The CBF, OEF and $CMRO_2$ were calculated with a noisy input function (circles) and separated input functions from the noisy arterial TAC by methods (A) (squares) and (B) (triangles), respectively. The orders of tracers $H_2^{15}O$–$^{15}O_2$ and $^{15}O_2$–$H_2^{15}O$ are indicated by white and black symbols, respectively.

4. Discussion and conclusion

We developed the separation methods of dual tracer coexistent blood TAC for the DARG protocol to avoid frequent blood sampling to calculate the quantitative CBF, OEF and $CMRO_2$ images. The present results showed that the values in CBF and $CMRO_2$ using input functions separated by the present method were reasonably accurate, i.e., the bias and deviation in CBF, OEF and $CMRO_2$ values were within 4%. When the dose of the second tracer was changed, the bias and deviation in CBF and $CMRO_2$ also changed; however, the sizes were within 5% when the ratio between AUCs in the first and second input functions was from half to two-fold. Further, the bias and deviation in the CBF and $CMRO_2$ values due to noise in the arterial TAC was less than 5% and was not severely enhanced against those from the noisy TIF.

The present results showed that the model-based function method (B) provided a more accurate value for CBF and/or $CMRO_2$ in both the $H_2^{15}O$–$^{15}O_2$ and the $^{15}O_2$–$H_2^{15}O$ protocols. The reason of the better performance of method (B) was the use of the entire period of data, although the expression of the model function was complex and the calculation took a longer time.

On the other hand, in the linear method (A), the arterial TAC was fitted with the linear function during a period of 120 to 180 s in the first phase, i.e. during the period after the shape of the first input function in the stable state, and the residual radioactivity was then estimated by extrapolating that function in the second phase. The bias and deviation in CBF and $CMRO_2$, calculated using separated input functions by method (A), were still within 4% and might be

acceptable for calculation. Thus, the present findings suggest that the dual tracer coexistent blood TAC can be separated by the linear function within a 4% accuracy. The advantages of method (A) over method (B) are easier implementation and faster computation. The linear regression program for the method (A) is readily available. On the other hand, for method (B), a computing framework for nonlinear fitting is required. We used the PAW environment for this purpose and fitting results might be different if another framework is employed. The benefit of faster computation could be minimized if a faster processor is used.

For the $^{15}O_2$–$H_2^{15}O$ protocol, the value of $CMRO_2$ was affected by the error in the separated input function, although the input function for calculating $CMRO_2$ was extracted in the first phase. This is because the $CMRO_2$ value was calculated not only from the input function and tissue TAC in the $^{15}O_2$ phase but also from the value of CBF that was estimated in the second phase and was affected by the separation error. However, the size of the error in $CMRO_2$ in $^{15}O_2$–$H_2^{15}O$ was less than 0.5% which is negligibly small. Further, the value for CBF in the $H_2^{15}O$–$^{15}O_2$ was unaffected by the error in separation, i.e., the CBF value was calculated exclusively in the first phase.

When the AUCs in the input function were almost the same between the first and second phases, the size of the bias in the value of CBF and $CMRO_2$ determined from the input function for the second phase tracer, i.e. CBF value for the $^{15}O_2$–$H_2^{15}O$ and $CMRO_2$ value for $H_2^{15}O$–$^{15}O_2$, was in the same range and was acceptable (figure 4). Moreover, the size of the bias was within a reasonable range when the ratio of the AUC between the first and second changed from half to two-fold. Practically, the present PET study on normal subjects showed that the fluctuation of the AUC of the input function was 20% when the tracer was administrated by the same procedure. This suggests that the degree of error due to the change in the ratio of the AUC of the input functions across subjects between the first and second phases could be within an acceptable range; further, the degree of error with regard to other error factors, such as delay or dispersion in input function was the same (Kudomi *et al* 2005).

Many PET scanners recently available are combined with CT scanners, and the patients reside deep inside the scanner housing during PET scanning. In this case, the length of the catheter tube must be long, which results in longer delay time and worse statistics in measured blood TAC. The size of errors as bias and deviation in CBF, OEF and $CMRO_2$ due to noise in the arterial blood TAC was less than 5% when the noise level was less than 10%. The 10% noise level corresponds to 100 cps in the measured water arterial TAC at its peak. Most devices monitoring arterial TAC can provide this level of statistics in practical examination for CBF, OEF and $CMRO_2$ evaluation for both 3SARG and DARG. Moreover, the degree of error in these values was not enhanced in comparison to that from noisy TIF. Thus, the separation procedure due to noise on the arterial TAC might not deteriorate the quantitative accuracy in CBF, OEF and $CMRO_2$.

The image quality in CBF and $CMRO_2$ by the DARG approach is influenced by the interval, relative dose, and order of the two administered tracers. Since the dose of the second tracer is less, a relatively larger amount of residual radioactivity from the first tracer remains during the image acquisition for the second tracer, and it results in the degradation of the quality of the image obtained during the second phase of the procedure. Thus, the dose of the second tracer should be as high as possible for the DARG approach in terms of the separation of the input function. However, when the dose of the second tracer is too high, the amount of random photons and dead time in the PET data would increase and the quantitative accuracy might be degraded. Further, the radiation dose increases for patients. These matters suggest that the amount and ratio of the tracer dose assumed in the present study might be appropriate for the DARG PET measurement.